IEEE Access
Multidisciplinary | Rapid Review | Open Access Journal

Received September 20, 2019, accepted October 13, 2019, date of publication October 23, 2019, date of current version November 6, 2019.

Digital Object Identifier 10.1109/ACCESS.2019.2949198

Impedance Modeling and SSR Analysis of DFIG Using Complex Vector Theory

XUEGUANG ZHANG, (Member, IEEE), YAGE ZHANG, RAN FANG, AND DIANGUO XU, (Fellow, IEEE)
School of Electrical Engineering and Automation, Harbin Institute of Technology, Harbin, China
Corresponding author: Xueguang Zhang (zxghit@126.com)

This work was supported by the National Key Research and Development Program of China under Grant 2018YFB0904000.

ABSTRACT Based on the complex vector theory, a more comprehensive doubly-fed induction generator (DFIG) impedance model under series compensated network, taking both outer loops and phase-locked loop (PLL) dynamic into consideration, is developed in stationary reference frame ($\alpha\beta$-frame). Then the complex vector-based impedance model is combined with the equivalent RLC circuit to intuitively and quantitatively explain the mechanism of sub-synchronous resonance (SSR) and its mitigation methods. The impact of the RSC controllers and series compensation level on the equivalent impedance and the SSR frequency of the DFIG system are analyzed. The mechanism of the two mitigating SSR methods, one is damping control and the other is virtual inductance control, is revealed based on the complex vector impedance model. Finally, the accuracy of the derived model and the theoretical analysis are verified by simulation.

INDEX TERMS Complex vector, doubly-fed induction generator (DFIG), equivalent RLC circuit, impedance modeling, sub-synchronous resonance (SSR).

I. INTRODUCTION

As a green renewable energy source, wind generation is playing an important role in addressing the present issue of global energy crisis. The doubly-fed induction generator (DFIG) has been widely used as the wind generator. However, in recent years, the interaction between the controllers of DFIG and the series-compensated grid tends to cause a new type of SSR, also named as sub-synchronous control interaction (SSCI) [1]–[4].

The commonly used stability methods are the eigenvalue analysis based on state-space modeling [5]–[8], and the impedance-based method [9]–[12]. It should be noted that these two methods are equivalent since the conversion can be easily made between them [13]. Recently, the impedance-based method is prevailing since it can be obtained through either analytical modeling or measurement [14]. What's more, the concept of impedance is closely and physically related to circuits, which may be easier for the interpretation of dynamics. The impedance model can be developed in dq domain by small signal linearization method [15], [16] or in sequence domain by harmonic linearization [17]–[22]. Later, the mathematical relations between the impedance models in the different domains are explicitly revealed base on the complex vector theory [23], and a unified impedance model is formulated [24]. Based on the unified complex vector impedance model, it can not only predict the stability impact of asymmetric dq-frame structures (e.g. the PLL and the outer controllers), but also reveal the frequency coupling effect in sequence domain [20], [21].

The establishment of a comprehensive and accurate model of DFIG is the basis of investigating the mechanism of SSR. A 20th order state-space model of the entire DFIG system is developed in [6], and modal analysis is performed in [7] to identify the four system modes. It is obvious that the model is complicated with high order and eigenvalue analysis is still a numerical method. It is difficult to reveal the mechanism of DFIG system losing stability under series compensated network compared with the impedance model. However, most of the previous impedance models are usually associated with model reductions since the complexity in deriving a detailed DFIG model [25]. e.g. [9] developed a DFIG impedance model with the inner control loop of rotor side controller (RSC) considered. Considering the influence of the PLL and the inner control loop of RSC, the sequence-domain impedance model of the DFIG was derived

The associate editor coordinating the review of this manuscript and approving it for publication was Meng Huang.

in [10], [11]. Recently, it is found that the outer loops have great influence on the SSR problem of grid-connected voltage source converters thus cannot be ignored [12]. The equivalent RLC impedance model of the DFIG system considering the outer loops is developed in [26], however, only the numerical result can be obtained due to the complexity of the system.Therefore, regarding SSR studies, it is necessary to establish an analytical DFIG impedance model with the RSC and GSC (including its outer and inner control loop), and the PLL dynamics considered.

Since the report of DFIG-related SSR event, plentiful results have been achieved. At present, it becomes widely accepted that DFIGs' controllers have evident effects on the SSR. The impact on SSR from wind speed, compensation degree and current loop proportional gains of RSC is analyzed in [9]. However, the Nyquist method can only provide qualitative results (i.e., stable or unstable) in a visual way. To facilitate intuitive and quantitative analysis of SSR, an aggregated RLC circuit model is proposed in [26]. Moreover, numerous SSR mitigation methods have been proposed by either utilizing ancillary devices [27], [28] or improving the original controls [29]–[35]. Since the RLC circuit is expressed in the stationary frame, it will be convenient for the application of the complex vector impedance model based on the stationary frame. Therefore, the mechanism of SSR and its mitigation methods can be intuitively analyzed by combining the complex vector-based impedance model with the equivalent RLC circuit.

Based on complex vector theory, a more accurate DFIG impedance model considering both power outer loop and PLL dynamic in $\alpha\beta$-frame is further deduced from the dq-frame model. Since the impedance model in $\alpha\beta$-frame can be naturally associated with the circuit, it is convenience to combine the DFIG impedance model with the equivalent RLC circuit. And it is beneficial to analyze the impact of controller parameters and series compensation level on the SSR frequency and equivalent impedance. The impedance-frequency curve reveals that the damping of the DFIG system decreases with the increase of frequency. Thereby, two methods for SSR mitigation is proposed based on the impedance-curves of the DFIG system. One method is the damping control, which is used to increase the system damping directly; the other method is the virtual inductance control, which is used to reduce the SSR frequency and increase the system damping indirectly. Therefore, the mechanism of the two ways mitigating SSR can be revealed intuitively and quantitatively based on the complex vector impedance model.

The rest of the paper is organized as follows. In Section II, based on the complex vector theory, the unified impedance model of the DFIG system considering both the RSC and the GSC in $\alpha\beta$-frame will be derived. In Section III analyzes the impact of controller parameters and grid parameters on the SSR characteristics of the DFIG system based on the equivalent RLC circuit. The mechanism of two ways mitigating SSR-the damping control and virtual inductance control-are revealed based on the complex vector impedance model in Section IV. The correctness of theoretical analysis is verified by simulation in Section V. Brief conclusions are drawn in Section VI.

II. IMPEDANCE MODELING OF DFIG USING COMPLEX VECTOR THEORY

The structure of the DFIG system investigated in this paper is depicted in Fig. 1.The whole system consists of the induction machine, both the rotor side converter (RSC) and grid side converter (GSC) as well as their inner and outer loop controllers, and the phase-locked loop (PLL). The main task of RSC is to control DFIG's stator output active and reactive power while the GSC controls the common dc bus voltage. $u_s(i_s)$, $u_r(i_r)$ represent the stator and rotor voltage (current), u_l, i_l represent the GSC voltage and current, u_{dc} is the dc bus voltage, i_g is the line current.

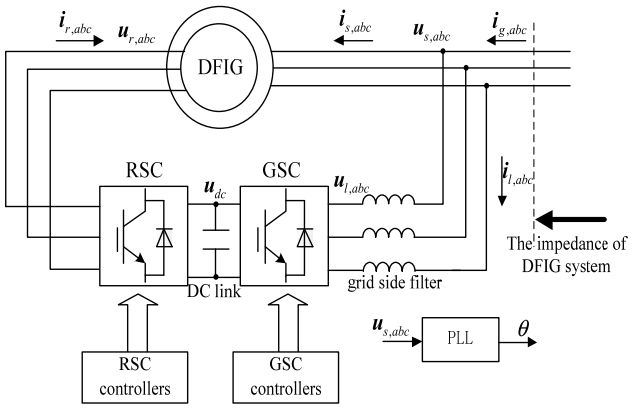

FIGURE 1. Structure diagram of the DFIG system.

A. COMPLEX VECTOR-BASED MODEL OF DFIG IN DQ-FRAME

The RSC and GSC mathematical model of the DFIG can be expressed by a two-by-two matrix in dq-frame [15], [16]. The representation of complex vector defined in dq-frame is shown as follows, where x represents the variables, X represents steady value and Δ represents small signal perturbation of the system.

$$\boldsymbol{x}_{dq} = x_d + jx_q \tag{1}$$

Add small-signal perturbation to (1), the physical variables in the system can be expressed by the following form:

$$\boldsymbol{X}_{dq} + \Delta\boldsymbol{x}_{dq} = (\mathrm{X}_d + \Delta x_d) + j(\mathrm{X}_q + \Delta x_q) \tag{2}$$

According to the above definition, the DFIG impedance model in complex vector form can be expressed as:

$$\begin{cases} \Delta\boldsymbol{u}^s_{s,dq} = [R_s + (s + j\omega)L_s]\Delta\boldsymbol{i}^s_{s,dq} + (s + j\omega)L_m\Delta\boldsymbol{i}^s_{r,dq} \\ \Delta\boldsymbol{u}^s_{r,dq} = [R_r + (s + j\omega_2)L_r]\Delta\boldsymbol{i}^s_{r,dq} + (s + j\omega_2)L_m\Delta\boldsymbol{i}^s_{s,dq} \end{cases} \tag{3}$$

where L_s, L_r represent the stator and rotor inductance, R_s, R_r represent the stator and rotor resistance, L_m represent the

mutual inductance, ω, ω_2 represent the synchronous and slip angular frequency, and the superscripts s and c indicate that the corresponding variable is in the system and controller coordinate, respectively.

Cascading the RSC power loop with the current loop, and then combining the small signal model of the stator active and reactive power, the impedance model of the RSC current inner loop and power outer loop in the form of complex vector is shown as follows:

$$\begin{aligned}\Delta \boldsymbol{u}^c_{r,dq} = {} & M(s)H(s)(\boldsymbol{U}^*_{s,dq}\Delta \boldsymbol{i}^c_{s,dq} + \boldsymbol{I}_{s,dq}\Delta \boldsymbol{u}^{c*}_{s,dq}) \\ & + (-H(s) + j\omega_2 L_r)\Delta \boldsymbol{i}^c_{r,dq} + j\omega_2 L_m \Delta \boldsymbol{i}^c_{s,dq} \end{aligned} \tag{4}$$

where $-\Delta P_s + j\Delta Q_s = \boldsymbol{U}^*_{s,dq}\Delta \boldsymbol{i}^c_{s,dq} + \boldsymbol{I}_{s,dq}\Delta \boldsymbol{u}^{c*}_{s,dq}$, $H(s) = k_{p,ir} + k_{i,ir}/s$ and $M(s) = k_{p,pq} + k_{i,pq}/s$ represent the PI controllers of RSC current and power loop. The symbol $*$ denotes the complex conjugate. If the RSC active and reactive controllers are different, then the impedance model is different from Equation (4), which will be shown in the Appendix.

The complex vector model of the PLL dynamic in dq-frame can be expressed as [24](details are shown in the appendix):

$$\begin{aligned}\Delta \boldsymbol{x}^c_{dq} &= \Delta \boldsymbol{x}^s_{dq} - 0.5jF(s)\boldsymbol{X}^s_{dq}\boldsymbol{\Delta u^s_{sq}} \\ &= \Delta \boldsymbol{x}^s_{dq} - 0.5F(s)\boldsymbol{X}^s_{dq}(\Delta \boldsymbol{u}^s_{s,dq} - \Delta \boldsymbol{u}^{s*}_{s,dq}) \end{aligned} \tag{5}$$

where $F(s)$ represents the closed-loop transfer function of the PLL, which can be expressed as:

$$F(\mathrm{s}) = \frac{k_{p,pll}s + k_{i,pll}}{s^2 + U_{sd}k_{p,pll}s + U_{sd}k_{i,pll}}$$

The complex vector model of the grid side filter and the grid side controllers (cascade the GSC voltage and current loop) are shown as follows:

$$\Delta \boldsymbol{u}^s_{l,dq} = -(sL + R_l + j\omega L)\Delta \boldsymbol{i}^s_{l,dq} + \Delta \boldsymbol{u}^s_{s,dq} \tag{6}$$

$$\Delta \boldsymbol{u}^c_{l,dq} = (-H_g(s) + j\omega L)\Delta \boldsymbol{i}^c_{l,dq} - N(s)H_g(s)\boldsymbol{\Delta u}_{dc} \tag{7}$$

where $\Delta \boldsymbol{u}_{dc} = \Delta u_{dc} + j0$, $H_g(s) = k_{p,il} + k_{i,il}/s$ and $N(s) = k_{p,dc} + k_{i,dc}/s$ represent the PI controllers of the GSC current and the dc voltage loop, respectively.

The complex vector model of the dc bus is expressed as:

$$\begin{aligned} sCU_{dc}\Delta \boldsymbol{u}_{dc} = {} & \boldsymbol{U}^*_{l,dq}\Delta \boldsymbol{i}^s_{l,dq} + \boldsymbol{U}_{l,dq}\Delta \boldsymbol{i}^{s*}_{l,dq} + \boldsymbol{I}^*_{l,dq}\Delta \boldsymbol{u}^s_{l,dq} \\ & + \boldsymbol{I}_{l,dq}\Delta \boldsymbol{u}^{s*}_{l,dq} - \boldsymbol{U}^*_{r,dq}\Delta \boldsymbol{i}^s_{r,dq} - \boldsymbol{U}_{r,dq}\Delta \boldsymbol{i}^{s*}_{r,dq} \\ & - \boldsymbol{I}^*_{r,dq}\Delta \boldsymbol{u}^s_{r,dq} - \boldsymbol{I}_{r,dq}\Delta \boldsymbol{u}^{s*}_{r,dq} \end{aligned} \tag{8}$$

B. COMPLEX VECTOR-BASED MODEL OF DFIG IN $\alpha\beta$-FRAME

The mathematical relationship between the dq-frame and $\alpha\beta$-frame impedance model can be revealed by complex transfer function and complex space vector [23]. Considering frequency translation, the dq-frame impedance model is transformed into the $\alpha\beta$-frame by this way [24]. For the process of frequency translation, specific explanations are given in [24], and a brief introduction is given here. The coupled complex vector impedance model in the dq-frame can be expressed as:

$$\begin{bmatrix} \Delta \boldsymbol{u}_{dq} \\ \Delta \boldsymbol{u}^*_{dq} \end{bmatrix} = \begin{bmatrix} Z_{dq,pp}(s) & Z_{dq,pn}(s) \\ Z_{dq,np}(s) & Z_{dq,nn}(s) \end{bmatrix} \begin{bmatrix} \Delta \boldsymbol{i}_{dq} \\ \Delta \boldsymbol{i}^*_{dq} \end{bmatrix} \tag{9}$$

The relation between the small signal physical variable in dq-frame and $\alpha\beta$-frame is shown as follows:

$$\begin{cases} \Delta \boldsymbol{x}_{dq} = e^{-j\omega t}\Delta \boldsymbol{x}_{\alpha\beta} \\ \Delta \boldsymbol{x}^*_{dq} = e^{j\omega t}\Delta \boldsymbol{x}^*_{\alpha\beta} \end{cases} \tag{10}$$

where $e^{-j\omega t}$, $e^{j\omega t}$ represent counterclockwise and clockwise rotation of the vector, respectively. Substituting (10) into (9), the coupled complex vector impedance model in the dq-frame can be expressed as:

$$\begin{aligned} & \begin{bmatrix} \Delta \boldsymbol{u}_{\alpha\beta} \\ e^{j2\omega t}\Delta \boldsymbol{u}^*_{\alpha\beta} \end{bmatrix} \\ & = \begin{bmatrix} e^{j\omega t} & 0 \\ 0 & e^{j\omega t} \end{bmatrix} \begin{bmatrix} Z_{dq,pp}(s) & Z_{dq,pn}(s) \\ Z_{dq,np}(s) & Z_{dq,nn}(s) \end{bmatrix} \begin{bmatrix} e^{-j\omega t}\Delta \boldsymbol{i}_{\alpha\beta} \\ e^{j\omega t}\Delta \boldsymbol{i}^*_{\alpha\beta} \end{bmatrix} \\ & = \begin{bmatrix} Z_{dq,pp}(s - j\omega) & Z_{dq,pn}(s - j\omega) \\ Z_{dq,np}(s + j\omega) & Z_{dq,nn}(s + j\omega) \end{bmatrix} \begin{bmatrix} \Delta \boldsymbol{i}_{\alpha\beta} \\ e^{j2\omega t}\Delta \boldsymbol{i}^*_{\alpha\beta} \end{bmatrix} \end{aligned} \tag{11}$$

For a given vector at the frequency ω_p, a frequency-coupled vector at the frequency $2\omega - \omega_p$ is yielded from (11). Hence, only when the frequency ω_p is above 2ω, there is a coupling between the positive-sequence and negative-sequence components. Otherwise, only the positive-sequence components at two different frequencies will be brought by the asymmetric transfer matrix.

The coupling frequency of the voltage and current vector in the $\alpha\beta$-frame changes after frequency translation. For the convenience of expression, let $s_2 = j2\omega - s$, then complex vector DFIG impedance model in $\alpha\beta$-frame is expressed as:

$$\begin{aligned} \begin{bmatrix} \Delta \boldsymbol{u}^s_{s,\alpha\beta} \\ \Delta \boldsymbol{u}^{s*}_{s,\alpha\beta} \end{bmatrix} = {} & \underbrace{\begin{bmatrix} R_s + sL_s & 0 \\ 0 & R_s + s_2L_s \end{bmatrix}}_{\boldsymbol{Gzs}} \begin{bmatrix} \Delta \boldsymbol{i}^s_{s,\alpha\beta} \\ \Delta \boldsymbol{i}^{s*}_{s,\alpha\beta} \end{bmatrix} \\ & + \underbrace{\begin{bmatrix} sL_m & 0 \\ 0 & s_2L_m \end{bmatrix}}_{\boldsymbol{Gzms}} \begin{bmatrix} \Delta \boldsymbol{i}^s_{r,\alpha\beta} \\ \Delta \boldsymbol{i}^{s*}_{r,\alpha\beta} \end{bmatrix} \end{aligned} \tag{12}$$

$$\begin{aligned} \begin{bmatrix} \Delta \boldsymbol{u}^s_{r,\alpha\beta} \\ \Delta \boldsymbol{u}^{s*}_{r,\alpha\beta} \end{bmatrix} = {} & \underbrace{\begin{bmatrix} R_r + (s - j\omega_r)L_r & 0 \\ 0 & R_r + (s_2 + j\omega_r)L_r \end{bmatrix}}_{\boldsymbol{Gzr}} \begin{bmatrix} \Delta \boldsymbol{i}^s_{r,\alpha\beta} \\ \Delta \boldsymbol{i}^{s*}_{r,\alpha\beta} \end{bmatrix} \\ & + \underbrace{\begin{bmatrix} (s - j\omega_r)L_m & 0 \\ 0 & (s_2 + j\omega_r)L_m \end{bmatrix}}_{\boldsymbol{Gzmr}} \begin{bmatrix} \Delta \boldsymbol{i}^s_{s,\alpha\beta} \\ \Delta \boldsymbol{i}^{s*}_{s,\alpha\beta} \end{bmatrix} \end{aligned} \tag{13}$$

Similarly, the complex vector impedance model of the PLL in the $\alpha\beta$-frame is expressed as:

$$\begin{aligned} \begin{bmatrix} \Delta \boldsymbol{x}^c_{y\alpha\beta} \\ \Delta \boldsymbol{x}^{c*}_{y\alpha\beta} \end{bmatrix} = {} & \begin{bmatrix} \Delta \boldsymbol{x}^s_{y\alpha\beta} \\ \Delta \boldsymbol{x}^{s*}_{y\alpha\beta} \end{bmatrix} - \frac{1}{2}\underbrace{\begin{bmatrix} F(s - j\omega) & 0 \\ 0 & F(s_2 + j\omega) \end{bmatrix}}_{\boldsymbol{F}} \\ & \times \underbrace{\begin{bmatrix} \boldsymbol{X}_{y\alpha\beta} & -\boldsymbol{X}_{y\alpha\beta} \\ \boldsymbol{X}^*_{y\alpha\beta} & -\boldsymbol{X}^*_{y\alpha\beta} \end{bmatrix}}_{\boldsymbol{X}} \boldsymbol{y} \begin{bmatrix} \Delta \boldsymbol{u}^s_{s,\alpha\beta} \\ \Delta \boldsymbol{u}^{s*}_{s,\alpha\beta} \end{bmatrix} \end{aligned} \tag{14}$$

The complex vector impedance model of the RSC controller in the $\alpha\beta$-frame is expressed as:

$$\begin{aligned}\begin{bmatrix}\Delta \boldsymbol{u}^{c}_{r,\alpha\beta}\\ \Delta \boldsymbol{u}^{c*}_{r,\alpha\beta}\end{bmatrix} &= \underbrace{\begin{bmatrix}-H(s-j\omega)+j\omega_2 L_r & 0\\ 0 & -H(s_2+j\omega)-j\omega_2 L_r\end{bmatrix}}_{\boldsymbol{G_{cir}}}\begin{bmatrix}\Delta \boldsymbol{i}^{c}_{r,\alpha\beta}\\ \Delta \boldsymbol{i}^{c*}_{r,\alpha\beta}\end{bmatrix}\\ &+\underbrace{\begin{bmatrix}0 & H(s-j\omega)M(s-j\omega)\boldsymbol{I}_{s,\alpha\beta}\\ H(s_2+j\omega)M(s_2+j\omega)\boldsymbol{I}^{*}_{s,\alpha\beta} & 0\end{bmatrix}}_{\boldsymbol{G_{cus}}}\begin{bmatrix}\Delta \boldsymbol{u}^{c}_{s,\alpha\beta}\\ \Delta \boldsymbol{u}^{c*}_{s,\alpha\beta}\end{bmatrix}\\ &+\underbrace{\begin{bmatrix}H(s-j\omega)M(s-j\omega)\boldsymbol{U}^{*}_{s,\alpha\beta}+j\omega_2 L_m & 0\\ 0 & H(s_2+j\omega)M(s_2+j\omega)\boldsymbol{U}_{s,\alpha\beta}-j\omega_2 L_m\end{bmatrix}}_{\boldsymbol{G_{cis}}}\\ &\times\begin{bmatrix}\Delta \boldsymbol{i}^{c}_{s,\alpha\beta}\\ \Delta \boldsymbol{i}^{c*}_{s,\alpha\beta}\end{bmatrix}\end{aligned}\tag{15}$$

Similarly, the complex vector impedance model of the grid side filter and GSC controller in the $\alpha\beta$-frame can be expressed as:

$$\begin{aligned}\begin{bmatrix}\Delta \boldsymbol{u}^{c}_{l,\alpha\beta}\\ \Delta \boldsymbol{u}^{c*}_{l,\alpha\beta}\end{bmatrix} &= \underbrace{\begin{bmatrix}-H_g(s-j\omega)+j\omega L & 0\\ 0 & -H_g(s_2+j\omega)-j\omega L\end{bmatrix}}_{\boldsymbol{G_{cig}}}\begin{bmatrix}\Delta \boldsymbol{i}^{c}_{l,\alpha\beta}\\ \Delta \boldsymbol{i}^{c*}_{l,\alpha\beta}\end{bmatrix}\\ &+\underbrace{\begin{bmatrix}-H_g(s-j\omega)N(s-j\omega) & 0\\ 0 & -H_g(s_2+j\omega)N(s_2+j\omega)\end{bmatrix}}_{\boldsymbol{G_{cvg}}}\\ &\times\begin{bmatrix}\Delta \boldsymbol{u}_{dc}\\ \Delta \boldsymbol{u}^{*}_{dc}\end{bmatrix}\end{aligned}\tag{16}$$

$$\begin{bmatrix}\Delta \boldsymbol{u}^{s}_{l,\alpha\beta}\\ \Delta \boldsymbol{u}^{s*}_{l,\alpha\beta}\end{bmatrix} = \underbrace{\begin{bmatrix}R_l+sL & 0\\ 0 & R_l+s_2L\end{bmatrix}}_{\boldsymbol{G_{zl}}}\begin{bmatrix}\Delta \boldsymbol{i}^{s}_{l,\alpha\beta}\\ \Delta \boldsymbol{i}^{s*}_{l,\alpha\beta}\end{bmatrix}+\begin{bmatrix}\Delta \boldsymbol{u}^{s}_{s,\alpha\beta}\\ \Delta \boldsymbol{u}^{s*}_{s,\alpha\beta}\end{bmatrix}\tag{17}$$

The complex vector impedance model of the dc bus module in the $\alpha\beta$-frame is expressed as:

$$\begin{aligned}&\underbrace{\begin{bmatrix}s-j\omega & 0\\ 0 & s_2+j\omega\end{bmatrix}CU_{dc}}_{\boldsymbol{G_{pdc}}}\begin{bmatrix}\Delta \boldsymbol{u}_{dc}\\ \Delta \boldsymbol{u}^{*}_{dc}\end{bmatrix}\\ &=\underbrace{\begin{bmatrix}\boldsymbol{U}^{*}_{l,\alpha\beta}\boldsymbol{U}_{l,\alpha\beta}\\ \boldsymbol{U}^{*}_{l,\alpha\beta}\boldsymbol{U}_{l,\alpha\beta}\end{bmatrix}}_{\boldsymbol{G_{pil}}}\begin{bmatrix}\Delta \boldsymbol{i}^{s}_{l,\alpha\beta}\\ \Delta \boldsymbol{i}^{s*}_{l,\alpha\beta}\end{bmatrix}+\underbrace{\begin{bmatrix}\boldsymbol{I}^{*}_{l,\alpha\beta}\boldsymbol{I}_{l,\alpha\beta}\\ \boldsymbol{I}^{*}_{l,\alpha\beta}\boldsymbol{I}_{l,\alpha\beta}\end{bmatrix}}_{\boldsymbol{G_{pvl}}}\\ &\times\begin{bmatrix}\Delta \boldsymbol{u}^{s}_{l,\alpha\beta}\\ \Delta \boldsymbol{u}^{s*}_{l,\alpha\beta}\end{bmatrix}-\underbrace{\begin{bmatrix}\boldsymbol{U}^{*}_{r,\alpha\beta}\boldsymbol{U}_{r,\alpha\beta}\\ \boldsymbol{U}^{*}_{r,\alpha\beta}\boldsymbol{U}_{r,\alpha\beta}\end{bmatrix}}_{\boldsymbol{G}}\boldsymbol{pir}\begin{bmatrix}\Delta \boldsymbol{i}^{s}_{r,\alpha\beta}\\ \Delta \boldsymbol{i}^{s*}_{r,\alpha\beta}\end{bmatrix}\\ &-\underbrace{\begin{bmatrix}\boldsymbol{I}^{*}_{r,\alpha\beta}\boldsymbol{I}_{r,\alpha\beta}\\ \boldsymbol{I}^{*}_{r,\alpha\beta}\boldsymbol{I}_{r,\alpha\beta}\end{bmatrix}}_{\boldsymbol{G_{pvr}}}\begin{bmatrix}\Delta \boldsymbol{u}^{s}_{r,\alpha\beta}\\ \Delta \boldsymbol{u}^{s*}_{r,\alpha\beta}\end{bmatrix}\end{aligned}\tag{18}$$

The RSC impedance model is the ratio of stator voltage to stator current. Substituting PLL dynamic Equation (14) into rotor control Equation (15) first, then combining stator voltage Equation (12) and rotor voltage Equation (13), and eliminating the vectors about rotor voltage and rotor current, the RSC inductance model can be obtained.

$$Y_{rsc} = \begin{bmatrix}\Delta \boldsymbol{i}^{s}_{s,\alpha\beta}\\ \Delta \boldsymbol{i}^{s*}_{s,\alpha\beta}\end{bmatrix}/\begin{bmatrix}\Delta \boldsymbol{u}^{s}_{s,\alpha\beta}\\ \Delta \boldsymbol{u}^{s*}_{s,\alpha\beta}\end{bmatrix} = B/A\tag{19}$$

where

$$\begin{aligned}A &= \boldsymbol{G_{zmr}}-\boldsymbol{G_{cis}}-(\boldsymbol{G_{zr}}-\boldsymbol{G_{cir}})\boldsymbol{G_{zs}}/\boldsymbol{G_{zms}}\\ B &= \boldsymbol{G_{cus}}-\boldsymbol{F}(\boldsymbol{G_{cir}}\boldsymbol{I_r}+\boldsymbol{G_{cus}}\boldsymbol{U_s}+\boldsymbol{G_{cis}}\boldsymbol{I_s}-\boldsymbol{U_r})/2\\ &\quad-(\boldsymbol{G_{zr}}-\boldsymbol{G_{cir}})/\boldsymbol{G_{zms}}\end{aligned}$$

Combining Equation (12)-(13) and (19), the following relationship can be acquired.

$$\begin{cases}\begin{bmatrix}\Delta \boldsymbol{u}^{s}_{r,\alpha\beta}\\ \Delta \boldsymbol{u}^{s*}_{r,\alpha\beta}\end{bmatrix} = \underbrace{((A-B\boldsymbol{G_{zs}})\boldsymbol{G_{zr}}+\boldsymbol{G_{zms}}\boldsymbol{G_{zmr}}B)/(A\boldsymbol{G_{zms}})}_{C}\\ \qquad\times\begin{bmatrix}\Delta \boldsymbol{u}^{s}_{s,\alpha\beta}\\ \Delta \boldsymbol{u}^{s*}_{s,\alpha\beta}\end{bmatrix}\\ \begin{bmatrix}\Delta \boldsymbol{i}^{s}_{r,\alpha\beta}\\ \Delta \boldsymbol{i}^{s*}_{r,\alpha\beta}\end{bmatrix} = \underbrace{(A-B\boldsymbol{G_{zs}})/(A\boldsymbol{G_{zms}})}_{D}\begin{bmatrix}\Delta \boldsymbol{u}^{s}_{s,\alpha\beta}\\ \Delta \boldsymbol{u}^{s*}_{s,\alpha\beta}\end{bmatrix}\end{cases}\tag{20}$$

The GSC impedance model is the ratio to stator voltage and grid side filter current. First substituting Equation (20) into Equation (18) to eliminate the vectors about rotor voltage and rotor current. Then substituting PLL dynamic Equation (14) into GSC control Equation (16), then combining grid side filter Equation (17) and dc bus Equation (18), the GSC inductance model can be obtained.

$$Y_{gsc} = \begin{bmatrix}\Delta \boldsymbol{i}^{s}_{l,\alpha\beta}\\ \Delta \boldsymbol{i}^{s*}_{l,\alpha\beta}\end{bmatrix}/\begin{bmatrix}\Delta \boldsymbol{u}^{s}_{s,\alpha\beta}\\ \Delta \boldsymbol{u}^{s*}_{s,\alpha\beta}\end{bmatrix} = (E+G)/(F-E\boldsymbol{G_{zl}})\tag{21}$$

where

$$\begin{aligned}E &= 1-\boldsymbol{G_{cvg}}\boldsymbol{G_{pvl}}/\boldsymbol{G_{pdc}}\\ F &= \boldsymbol{G_{cig}}+\boldsymbol{G_{cvg}}\boldsymbol{G_{pil}}/\boldsymbol{G_{pdc}}\\ G &= \boldsymbol{F}(\boldsymbol{G_{cig}}\boldsymbol{I_l}-\boldsymbol{U_l})/2+\boldsymbol{G_{cvg}}\boldsymbol{G_{pir}}D/\boldsymbol{G_{pdc}}+\boldsymbol{G_{cvg}}\boldsymbol{G_{pvr}}C/\boldsymbol{G_{pdc}}\end{aligned}$$

The DFIG system impedance consists of two parallel branches: one is the induction generator and the RSC, and the other is the GSC and the filter. Therefore, the whole DFIG impedance can be obtained as follows:

$$Z_{dfig} = (Y_{rsc}+Y_{gsc})^{-1} = \begin{bmatrix}Z_{pp} & Z_{cou\_p}\\ Z_{cou\_n} & Z_{nn}\end{bmatrix}\tag{22}$$

where, Z_{pp}, Z_{nn} represent the complex vector of the positive and negative sequence impedance, $Z_{cou,p}$, $Z_{cou,n}$ represent the coupling impedance introduced by the frequency coupling.

In order to verify the correctness of the impedance model proposed in this paper, the frequency sweep method are implemented for the DFIG system under sub/super synchronous conditions. Principle of frequency sweep method

has been specified in [11], [12], [20]. At the point of common coupling (PCC), inject a small voltage perturbation signals at specific frequency superposed on the operating condition. Then extract the perturbed small-signal current, and apply FFT analysis on its α-axis and β-axis value under the corresponding frequency. Changing the voltage perturbation frequency and repeating the above steps, the DFIG system impedance can be got at each frequency point. With the parameters in Table 1 and Table 2 of the Appendix, the comparison of the theoretical calculation and simulation measurement results of DFIG output impedance in $\alpha\beta$-frame are shown in Fig. 2, red curve is the theoretical calculation results and the blue circles are the simulation measurement results. In the range of 5-1000Hz, the calculated results of the positive and negative sequence impedance of the DFIG are basically consistent with the measurement results, which means that the accuracy of the DFIG frequency coupling models can be validated. It can be seen in Fig. 2 that the amplitude of the coupling impedance introduced by the frequency coupling is about 20 dB smaller than the corresponding sequence impedance in the whole frequency range. Therefore, the coupling impedance can be ignored in the analysis. Especially at the sub-synchronous frequency, the amplitude of the coupling term is very small, it has little effect on the system impedance, the influence of it is no longer considered in subsequent studies.

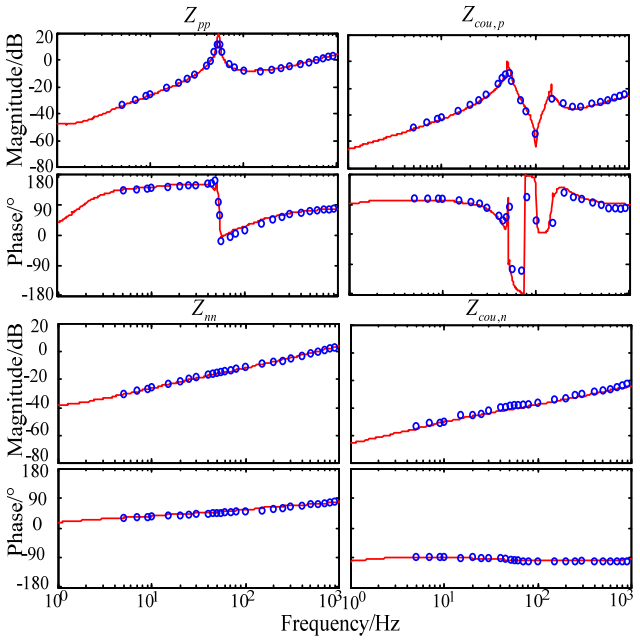

FIGURE 2. The comparison of the theoretical calculation and simula-tion measurement results of DFIG output impedance in $\alpha\beta$-frame.

III. SUB-SYNCHRONOUS RESONANCE ANALYSIS BASED ON THE COMPLEX VECTOR IMPEDANCE MODEL

The DFIG-based wind power system can be equivalent to a series RLC resonant circuit near the resonant frequency. The SSR severity of the system can be determined by the frequency characteristic curve of the DFIG input impedance [26]. Based on the physical interpretation of the complex vector impedance model, the equivalent RLC series resonant circuits can be applied to analyze the impact of different phase sequence, controller parameters and grid parameters on SSR.

It should be noted that the magnitude of the impedance in GSC is much larger than the RSC at the interested SSR region, therefore the impedance of RSC is dominant [9]. The effect of the GSC on the SSR damping and frequency is much less than that of the RSC. In [36], it is pointed out that the larger proportional and integral gains of the PLL, and the more likely the SSR will occur. The analysis of this paper is consistent with it. Therefore, the impact of the GSC and the PLL will not be considered in the following studies.

A. SSR ANALYSIS BASED ON THE EQUIVALENT RLC SERIES CIRCUIT

The equivalent circuit of the DFIG system under series compensation is shown in Fig. 3. L_{sum} represents the equivalent inductance of the whole DFIG system, R_{sum} represents the equivalent resistance of the whole DFIG system; C_g represents the capacitance in the series compensated grid. U_{grid} represents the equivalent voltage source of the grid. U_{dfig} represents the equivalent voltage source of the DFIG.

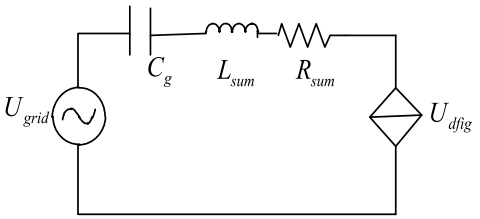

FIGURE 3. Equivalent RLC circuits diagram of grid-connected DFIG system.

When the DFIG is connected to the series-compensated grid, the equivalent inductance, resistance and SSR frequency of the system are expressed as:

$$L_{sum} = L_{dfig} + L_g = \mathrm{Im}(Z_{pp}) + L_g \tag{23}$$

$$R_{sum} = R_{dfig} + R_g = \mathrm{Re}(Z_{pp}) + R_g \tag{24}$$

$$f_{SSR} = 1/(2\pi\sqrt{(L_{dfig} + L_g)C_g}) \tag{25}$$

where, L_{dfig} and L_g represent the equivalent inductance of the DFIG and the grid respectively, R_{dfig} and R_g represent the equivalent resistance of the DFIG and the grid respectively. Im and Re represent the imaginary and real part of Z_{PP}.

The positive and negative sequence equivalent impedance of the series-compensated grid in the $\alpha\beta$-frame is expressed as:

$$Z_{g,p} = Z_{g,n} = R_g + sL_g + \frac{1}{sC_g} \tag{26}$$

Combining the impedance model of the DFIG and the series-compensated grid in the $\alpha\beta$-frame, the equivalent impedance curves of the grid-connected DFIG system varying with frequency can be drawn in one diagram.

The intersection frequency of the equivalent inductance and capacitance is the SSR frequency of the grid-connected DFIG system. If the equivalent resistance of the system under the intersection frequency is positive, the SSR is stabilized; if the equivalent resistance of the system under the intersection frequency is negative, unstable SSR will occur.

B. ANALYSIS OF SSR IN DIFFERENT PHASE SEQUENCE

The reasons for the occurrence of SSR in the grid-connected DFIG system are shown in this section. At the SSR frequency, the rotor speed is less than the synchronous speed, thus the rotor side resistance of DFIG $R_{\rm rsc}$ behaves like a negative resistance viewed from the stator terminals. Once the negative resistance exceeds the total resistances of the stator and the network, the unstable SSR will occur [33].

In the case of positive sequence, the expression of the rotor side resistance of DFIG viewed from the stator terminals at the SSR frequency is expressed as:

$$R_{r,eq} = \frac{R_{rsc}}{\sigma_p}, \quad \sigma_p = \frac{\omega_{ssr} - \omega_r}{\omega_{ssr}} \tag{27}$$

where, σ_p represents the slip of the machine at frequency $\omega_{\rm ssr}$. When $\sigma_p(s) < 0$, $R_{r,eq}$ is negative, if the negative resistance exceeds the total resistances of the stator and the network, the whole system will exhibit negative resistance feature and the unstable SSR will occur.

In the case of negative sequence, the expression of the rotor side resistance of the DFIG system viewed from the stator terminals at the SSR frequency is expressed as:

$$R_{r,eq} = \frac{R_{rsc}}{\sigma_n}, \quad \sigma_n = \frac{\omega_{ssr} + \omega_r}{\omega_{ssr}} \tag{28}$$

It is obvious that σ_n is always greater than zero. That is, the rotor side equivalent resistance of negative sequence is always positive at the SSR frequency, which means that the probability of SSR is small.

With the parameters in Table 1 and Table 2 of the Appendix, the positive and negative sequence equivalent impedance (inductance, capacitance and resistance) of the system changing with frequency are drawn in Fig. 4. The intersection frequency of inductance and capacitance of the DFIG system is $f_{ssr} = 18Hz$ in positive sequence. The system damping is negative at that frequency, so the system is prone to divergent oscillation. Whereas, the system damping in negative sequence is always positive, which means the risk of negative sequence divergent oscillation is minimal. Therefore, only the positive sequence impedance is analyzed in the subsequent studies.

C. IMPACT OF CONTROLLERS AND GRID PARAME-TERS ON SSR

Fig. 5 shows the system impedance-frequency curves when the proportional gain of RSC current controller $k_{\rm p,ir}$ changes. With the increase of $k_{\rm p,ir}$, the equivalent resistance of the system decreases in the SSR region, indicating that the system is more prone to unstable SSR; the equivalent inductance of the system increases, indicating that the SSR frequency of the system decreases.

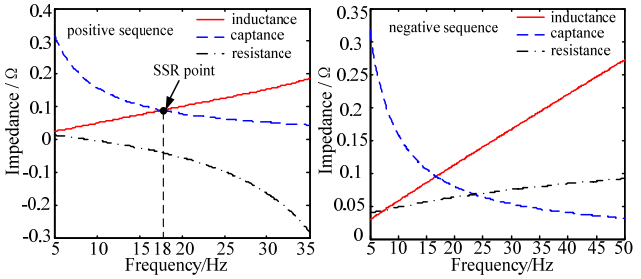

FIGURE 4. System impedance-frequency curves.

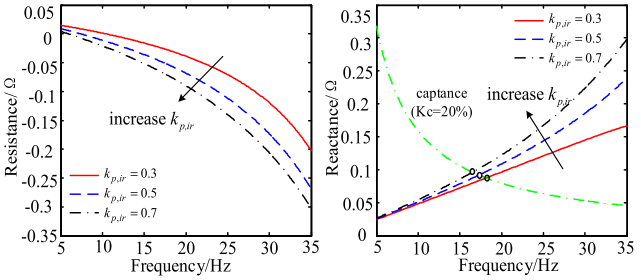

FIGURE 5. System impedance-frequency curves when proportional gain of RSC current controller $k_{p,ir}$ changes.

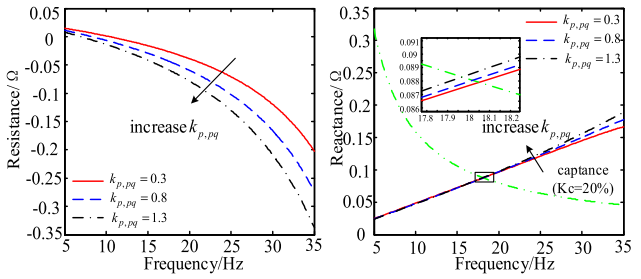

FIGURE 6. System impedance-frequency curves when proportional gain of the RSC power controller $k_{p,pq}$ changes.

The impact of the proportional gain of the RSC power controller on the frequency and damping of SSR is shown in Fig. 6. With the increase of $k_{\rm p,pq}$, the positive sequence equivalent resistance decreases in the SSR region, indicating that the system is more prone to unstable SSR; the equivalent inductance of the system increases slightly, indicating that the SSR frequency of the system decreases slightly.

Fig. 7 shows the system reactance-frequency curves when the series compensation level Kc changes. With the increase of Kc, the equivalent capacitance increases and the SSR frequency increases. Since the equivalent resistance of the system decreases with the frequency increases in the SSR region, the system is more prone to unstable SSR.

IV. DAMPING OF SSR

It is clearly depicted in Fig. 4 that the equivalent resistance of the DFIG system increases with the decrease of resonance frequency in the SSR region. Hence, it is easy to think that the SSR can be mitigated by increasing the equivalent resistance

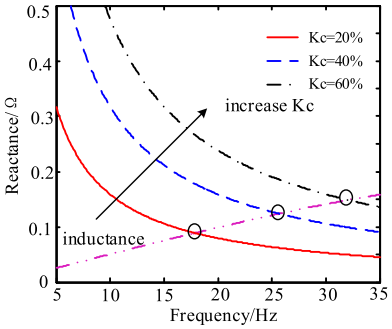

FIGURE 7. System reactance-frequency curves when the series com-pensation level Kc changes.

or reducing the resonance frequency. Therefore, damping control can be used to increase the system damping and virtual inductance control can be used to reduce the resonance frequency. Besides, these two methods can be combined with RLC circuit to quantitatively analyze the effect of additional control methods on system damping.

A. SSR DAMPING CONTROL

The auxiliary damping controller can increase the damping of the DFIG system in the SSR region, which can effectively improve the system's stability. The RSC impedance is the dominant feature of the entire impedance model. The system damping can be improved by increasing the stator resistance, which is equivalent to introducing the stator current signal into RSC current controller, and it is easy to apply the auxiliary damping control. The RSC damping controllers are shown in Fig. 8. The high-pass filter G_{HPF} is used to filter the stator current steady state components, which is beneficial to eliminate the effect of additional damping control on the operating point of the system. The first-order high-pass filter is adopted in this paper, and the expression is shown in (29). Considering the frequency range of the extracted resonant signal, the time constant of the high-pass filter T_h is set to 0.5.

$$G_{HPF} = \frac{T_h s}{T_h s + 1} \tag{29}$$

where K_{damp} represents the damping gain. Fig. 9 shows system resistance-frequency curves when the damping gain K_{damp} changes. When the auxiliary damping control is introduced into RSC, the positive sequence equivalent damping of the DFIG system increases, indicating that the system's ability to suppress SSR is strengthened. However, at a higher frequency range, the damping of the DFIG system decreases, which is not conducive to the stability of the system. It is due to the negative effects that K_{damp} can't be too large, which limits the effect of the improved controllers to mitigate the SSR.

B. VIRTUAL INDUCTANCE CONTROL

It can be found in Fig. 4 that the damping of the system increases with the decreases of resonance frequency in the SSR region. Therefore, it can be considered to improve the system stability by reducing the resonance frequency.

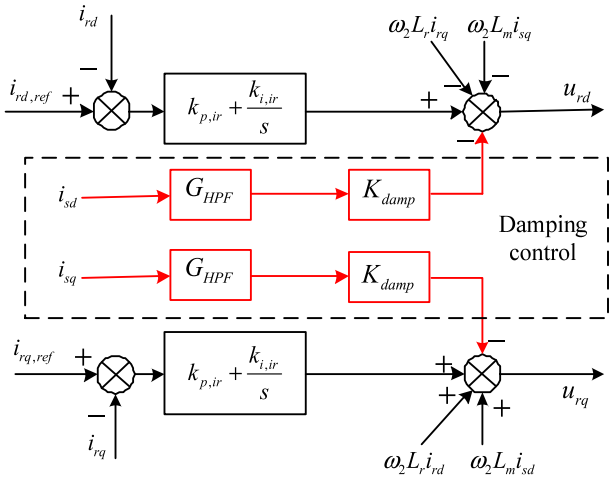

FIGURE 8. Block diagram of RSC current loop with damping control.

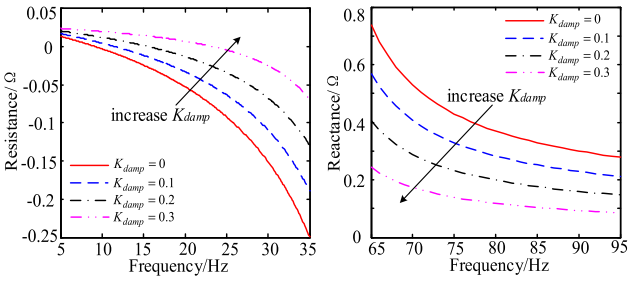

FIGURE 9. System resistance-frequency curves when the damping gain K_{damp} changes.

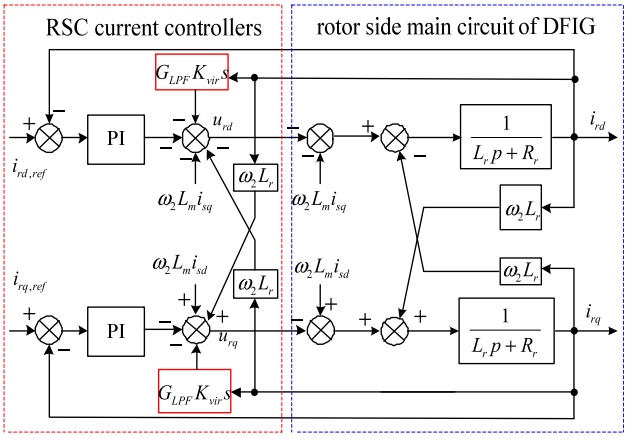

FIGURE 10. Block diagram of RSC current loop with virtual inductance control.

By increasing the equivalent inductance of the DFIG system, the frequency of the SSR can be reduced. The equivalent impedance of the DFIG is dominated by the RSC, therefore it is simple and convenient to introduce virtual inductance into the RSC. Fig. 10 shows the block diagram of RSC current loop with virtual inductance control.

In Fig. 10, G_{LPF} represents the low-pass filter transfer function. Because the differential term is difficult to be implemented in the controller, the first-order low-pass filter is adopted with the cutoff frequency of 1000Hz.

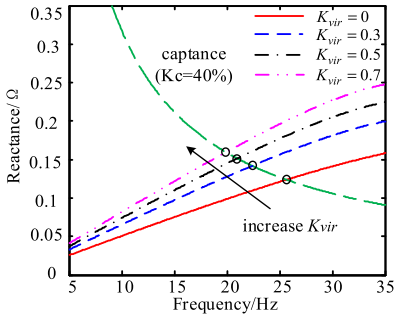

FIGURE 11. System resistance-frequency curves when the virtual in-ductance gain K_{vir} changes.

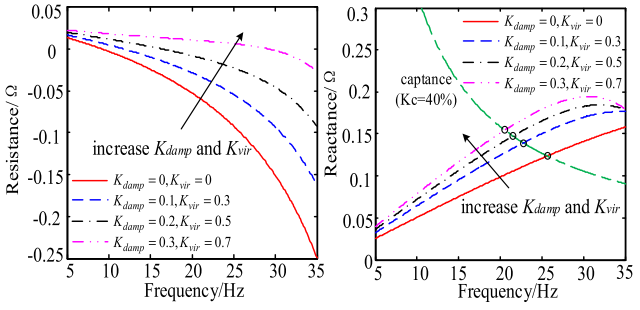

FIGURE 12. System impedance-frequency curves when the virtual in-ductance gain K_{vir} and the damping gain K_{damp} changes.

K_{vir} represents the virtual inductance gain, and Fig. 11 shows system reactance-frequency curves when virtual inductance gain K_{vir} changes. With the increase of K_{vir}, the system equivalent inductance increases, indicating that the resonance frequency decreases. Subsequently the equivalent damping of the system improved indirectly, which improves the system's stability.

C. DAMPING AND VIRTUAL INDUCTANCE CONTROL

Introducing both damping control and virtual inductance control into the RSC simultaneously, there will be a better effect on SSR mitigation. On one hand, the SSR frequency is reduced; on the other hand, the DFIG system equivalent resistance increases. Fig. 12 shows that the system impedance-frequency curves when virtual inductance gain K_{vir} and the damping gain K_{damp} change. With the virtual inductance control and damping control taking effect simultaneously, the equivalent damping of the DFIG system is improved, and the SSR frequency is effectively reduced, which is equivalent to further increasing the damping of the DFIG system. Therefore, the damping control and virtual inductance control is better to apply simultaneously.

V. SIMULATION VERIFICATION

To validate the accuracy of the proposed impedance model as well as the correctness of the theoretical analysis based on the complex vector impedance model, a 1.5MW DFIG detail model is built in MATLAB/Simulink. The parameters of the DFIG system used in the simulation are listed in table 1 and table 2 of the Appendix.

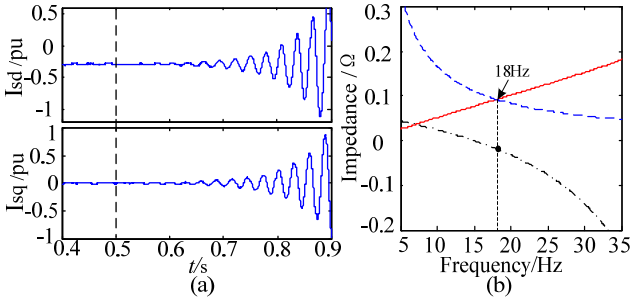

FIGURE 13. (a) Stator dq current waveform by increasing the propor-tional gain of current controller $k_{p,ir}$. (b) DFIG system impedance-frequency curves.

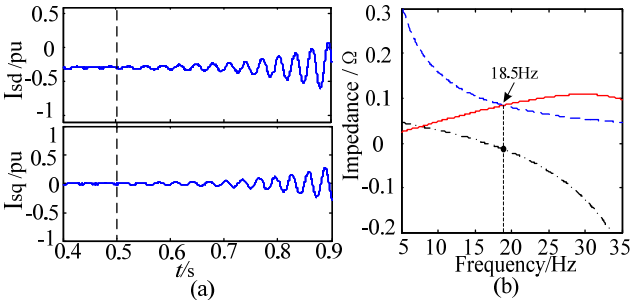

FIGURE 14. (a) Stator dq current waveform by increasing the propor-tional gain of the RSC power controller $k_{p,pq}$.(b) DFIG system impedance-frequency curves.

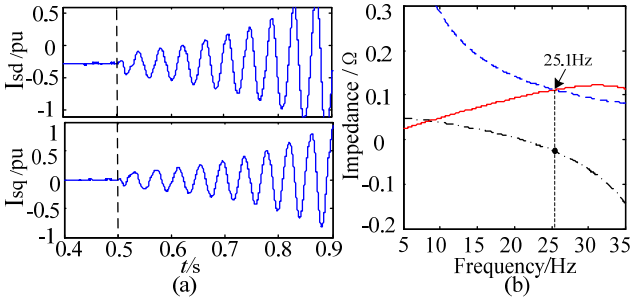

FIGURE 15. (a) Stator dq current waveform by increasing series com-pensation level Kc (b) DFIG system impedance-frequency curves.

A. IMPACT OF CONTROLLERS AND GRID PARAME-TERS

Fig. 13 shows the stator current waveforms of DFIG at $\omega = 0.7$ and 20% compensation level. Proportional gain of RSC current controller changes from 0.2 to 0.35 at 0.5s, and the waveform of stator current deteriorate because of SSR. The frequency of SSR is about 18Hz. The simulation result accords with the analysis of the RLC impedance model.

Fig. 14 depicts the stator current waveforms at $\omega = 0.7$ and 20% compensation level. Proportional gain of RSC power controller changes from 0.3 to 0.9 at 0.5s, and DFIG stator current starts to oscillate at the frequency about 18.5Hz. The simulation results accords with the analysis of the RLC impedance model.

Fig. 15 presents the simulation results when the compensation level changes from 20% to 40% at 0.5s. The stator current begins to oscillate after 0.5s, and the frequency of SSR

is about 25Hz. The simulation result proves that the higher the compensation level, the more unstable the system will be. The simulation result accords with the analysis of the RLC impedance model.

B. PERFORMANCE OF DAMPING AND VIRTUAL IN-DUCTANCE CONTROL

Under the condition that the compensation level is 40% and the proportional gain of the RSC power controller is 0.3, the proportional gain of the RSC current controller changes from 0.1 to 0.25 at 0.5s. The stator current waveforms of DFIG with and without the virtual inductance control are shown in Fig. 16. After the introduction of virtual inductance control, the frequency of SSR drops from 25Hz to 21Hz, which indirectly increases the system's equivalent damping and slows down the divergence speed of the system.

Under the condition that the compensation level is 40% and the proportional gain of the RSC power controller is 0.3, the proportional gain of the RSC current controller changes from 0.1 to 0.3 at 0.5s. The simulation process is divided into four segments: a) no mitigation strategy; b) with only the damping control; c) with only the virtual inductance control; d) with the combined damping and virtual inductance control. The current waveform of phase A is shown in Fig. 17.

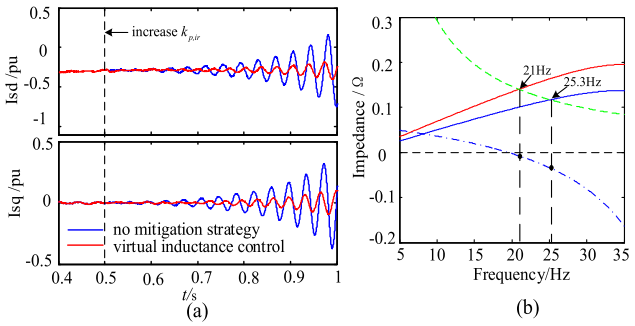

FIGURE 16. (a) Stator dq current waveform with/without virtual induc-tance control by increasing $k_{p,ir}$ (b) DFIG system impedance-frequency curves.

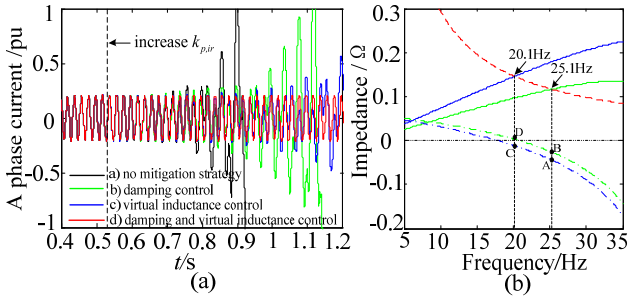

FIGURE 17. (a) A phase current waveform with different control modes by increasing the proportional gain of RSC current controller $k_{p,ir}$ (b) DFIG system impedance-frequency curves.

As can be seen from Fig. 17, when no mitigation strategy is applied, the damping of the system is at point A, where the resistance is negative, and the frequency of SSR is about 25Hz. With only the damping control, the system damping is at point B, where the resistance increases but it's still negative, and the divergence speed of the system slows down. With only the virtual inductance control, the system damping is at point C, where the frequency of SSR drops from 25Hz to 20Hz, which indirectly increases the system's damping and slows down the divergence speed of the system. With the combined damping and virtual inductance control, the damping of the system is at point D, where the new resistance becomes positive, thereby successfully suppressing the originally unstable SSR.

Under the condition that the compensation level is 40% and the proportional gain of the RSC current controller is 0.1, the proportional gain of the RSC power controller changes from 0.3 to 0.9 at 0.5s. Fig. 18(a) shows the stator dq current waveform with/without coordinated improved control by increasing the proportional gain of the RSC power controller $k_{p,pq}$, and Fig. 18(b) shows the DFIG impedance-frequency curves. It can be seen in Fig. 18 that without the coordinated improved control (damping and virtual inductance control), the stator dq current divergences (blue curves in Fig. 18(a)) when $k_{p,pq}$ increases from 0.3 to 0.9, and the damping of the system changes from point A to point B(from positive to negative). Then if the coordinated improved control is applied, the stator dq axis current is stable (red curves in Fig. 18(a)) when $k_{p,pq}$ increases from 0.3 to 0.9, and the damping of the system changes from point B to point C(from negative to positive), the system returns to stable.

Under the condition that the proportional gain of the RSC current controller is 0.2 and the proportional gain of the RSC power controller is 0.3, the compensation level changes from 20% to 40% at 0.5s. Fig. 19(a) shows the stator dq current waveform with/without coordinated improved control by increasing series compensation level Kc and Fig. 19(b) shows the DFIG impedance-frequency curves. It can be seen in Fig. 19 that without the coordinated improved control, the stator dq current divergences (blue curves in Fig. 19(a)) when the com-pensation level changes from 20% to 40%, and the damping of the system changes from point A to point B(from positive to negative). Then if the coordinated improved control is applied, the stator dq current is stable (red curves in Fig. 19(a)) when the compensation level changes from 20% to 40%, and the damping of the system changes

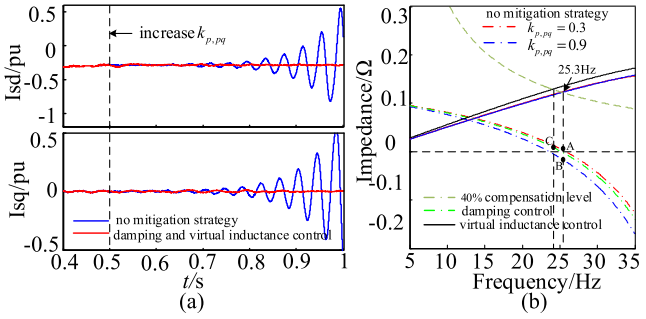

FIGURE 18. (a) Stator dq current waveform with/without coordinated improved control by increasing the proportional gain of the RSC power controller $k_{p,pq}$ (b) DFIG system impedance-frequency curves.

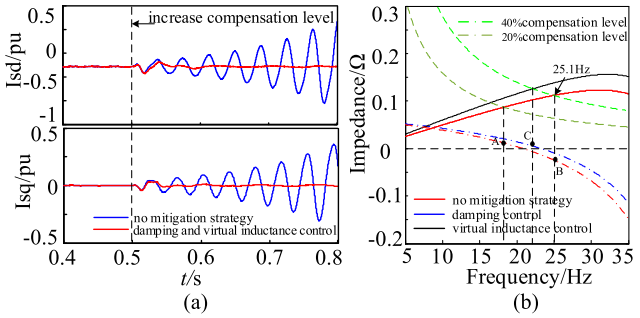

FIGURE 19. (a) Stator dq current waveform with/without coordinated improved control by increasing series compensation level Kc (b) DFIG system impedance-frequency curves.

from point B to point C (from negative to positive), the system returns to stable.

Therefore, the damping control and virtual inductance control has the ability mitigate SSR, and the influence of the two methods on system damping can be analyzed intuitively by the equivalent RLC circuit based on the complex vector impedance model proposed in this paper.

VI. CONCLUSION

The contribution of this paper is to establish the unified impedance model of DFIG by using complex vector theory, and to reveal the mechanism of SSR and its mitigation methods combining with the equivalent RLC circuit. It has following distinguished features:

i) Based on the mathematical relations between the dq-frame and $\alpha\beta$-frame impedance model, a unified impedance model of DFIG has further been deduced using complex vector theory. It fully considers the outer loop controls and PLL dynamics and thus can be used for the accurate evaluation of SSR.

ii) Damping control can increase the damping of SSR region, whereas the virtual inductance control has the potential to reduce the SSR frequency and indirectly increase the system's damping.

TABLE 1. Parameters of DFIG system and grid.

Parameters	Symbol	Value
DFIG Base capacity	S_B	1.5MVA
DFIG Nominal voltage	V_B	690V
Rated frequency	f_B	50Hz
Rotor inductance	L_r	3.06 p.u.
Stator inductance	L_s	3.08 p.u.
Rotor resistance	R_r	0.016 p.u.
Stator resistance	R_s	0.023 p.u.
Mutual inductance	L_M	2.9 p.u.
Grid inductance	L_g	0.5 p.u.
Grid resistance	R_g	0.04 p.u.
GSC filter inductance	L_f	0.3 p.u.
Grid capacitance	C_g	0.1 p.u.

The unified impedance model not only helps the analysis of the interaction between DFIG system and series-compensated grid, but also has implications to the analysis of oscillations of the DFIG system under other circumstances.

APPENDIX

See Tables 1 and 2.

TABLE 2. Parameters of controllers.

Controller	Proportional gains	Integral gains
RSC current controller	$k_{p,ir}=0.1$	$k_{i,ir}=10$
RSC power controller	$k_{p,pq}=0.3$	$k_{i,pq}=10$
GSC current controller	$k_{p,ig}=2$	$k_{i,ig}=10$
GSC dc voltage loop	$k_{p,dc}=0.8$	$k_{i,dc}=10$
PLL	$k_{p,pll}=10$	$k_{i,pll}=30$

REFERENCES

[1] R. Cardenas, R. Pena, S. Alepuz, and G. Asher, "Overview of control systems for the operation of DFIGs in wind energy applications," *IEEE Trans. Ind. Electron.*, vol. 60, no. 7, pp. 2776–2798, Jul. 2013.

[2] X. Xie, X. Zhang, H. Liu, H. Liu, Y. Li, and C. Zhang, "Characteristic analysis of subsynchronous resonance in practical wind farms connected to series-compensated transmissions," *IEEE Trans. Energy Convers.*, vol. 32, no. 3, pp. 1117–1126, Sep. 2017.

[3] W. Ren and E. Larsen, "A refined frequency scan approach to subsynchronous control interaction (SSCI) study of wind farms," *IEEE Trans. Power Syst.*, vol. 31, no. 5, pp. 3904–3912, Sep. 2016.

[4] H. Liu, X. Xie, X. Gao, H. Liu, and Y. Li, "Stability analysis of SSR in multiple wind farms connected to series-compensated systems using impedance network model," *IEEE Trans. Power Syst.*, vol. 33, no. 3, pp. 3118–3128, May 2018.

[5] J. Hu, Y. Huang, D. Wang, H. Yuan, and X. Yuan, "Modeling of grid-connected DFIG-based wind turbines for DC-link voltage stability analysis," *IEEE Trans. Sustain. Energy*, vol. 6, no. 4, pp. 1325–1335, Oct. 2015.

[6] L. Fan, R. Kavasseri, Z. L. Miao, and C. Zhu, "Modeling of DFIG-based wind farms for SSR analysis," *IEEE Trans. Power Del.*, vol. 25, no. 4, pp. 2073–2082, Oct. 2010.

[7] L. Fan, C. Zhu, Z. Miao, and M. Hu, "Modal analysis of a DFIG-based wind farm interfaced with a series compensated network," *IEEE Trans. Energy Convers.*, vol. 26, no. 4, pp. 1010–1020, Dec. 2011.

[8] L. Wang, X. Xie, Q. Jiang, H. Liu, Y. Li, and H. Liu, "Investigation of SSR in practical DFIG-based wind farms connected to a series-compensated power system," *IEEE Trans. Power Syst.*, vol. 30, no. 5, pp. 2772–2779, Sep. 2015.

[9] Z. Miao, "Impedance-model-based SSR analysis for type 3 wind generator and series-compensated network," *IEEE Trans. Energy Convers.*, vol. 27, no. 4, pp. 984–991, Dec. 2012.

[10] I. Vieto and J. Sun, "Sequence impedance modeling and analysis of Type-III wind turbines," *IEEE Trans. Energy Convers.*, vol. 33, no. 2, pp. 537–545, Jun. 2018.

[11] Y. Xu, H. Nian, T. Wang, L. Chen, and T. Zheng, "Frequency coupling characteristic modeling and stability analysis of doubly fed induction generator," *IEEE Trans. Energy Convers.*, vol. 33, no. 3, pp. 1475–1486, Sep. 2018.

[12] W. Liu, Z. Lu, X. Wang, and X. Xie, "Frequency-coupled admittance modelling of grid-connected voltage source converters for the stability evaluation of subsynchronous interaction," *IET Renew. Power Gener.*, vol. 13, no. 2, pp. 285–295, Feb. 2019.

[13] M. Amin and M. Molinas, "Small-signal stability assessment of power electronics based power systems: A discussion of impedance- and eigenvalue-based methods," *IEEE Trans. Ind. Appl.*, vol. 53, no. 5, pp. 5014–5030, Sep./Oct. 2017.

[14] C. Zhang, M. Molinas, A. Rygg, and X. Cai, "Impedance-based analysis of interconnected power electronics systems: Impedance network modeling and comparative studies of stability criteria," *IEEE J. Emerg. Sel. Topics Power Electron.*, to be published.
[15] R. Fang, W. Chen, X. Zhang, and D. Xu, "Improved virtual inductance based control strategy of DFIG under weak grid condition," in *Proc. Int. Power Electron. Conf. (IPEC-Niigata-ECCE Asia)*, May 2018, pp. 4213–4219.
[16] B. Wen, D. Boroyevich, R. Burgos, P. Mattavelli, and Z. Shen, "Analysis of D-Q small-signal impedance of grid-tied inverters," *IEEE Trans. Power Electron.*, vol. 31, no. 1, pp. 675–687, Jan. 2016.
[17] J. Sun, "Small-signal methods for AC distributed power systems—A review," *IEEE Trans. Power Electron.*, vol. 24, no. 11, pp. 2545–2554, Nov. 2009.
[18] J. Sun, Z. Bing, and K. J. Karimi, "Input impedance modeling of multipulse rectifiers by harmonic linearization," *IEEE Trans. Power Electron.*, vol. 24, no. 12, pp. 2812–2820, Dec. 2009.
[19] M. Cespedes and J. Sun, "Impedance modeling and analysis of grid-connected voltage-source converters," *IEEE Trans. Power Electron.*, vol. 29, no. 3, pp. 1254–1261, Mar. 2014.
[20] A. Rygg, M. Molinas, C. Zhang, and X. Cai, "A modified sequence-domain impedance definition and its equivalence to the DQ-domain impedance definition for the stability analysis of AC power electronic systems," *IEEE J. Emerg. Select. Topics Power Electron.*, vol. 4, no. 4, pp. 1383–1396, Dec. 2016.
[21] M. K. Bakhshizadeh, X. Wang, F. Blaabjerg, J. Hjerrild, L. Kocewiak, C. L. Bak, and B. Hesselbaek"Couplings in phase domain impedance modeling of grid-connected converters," *IEEE Trans. Power Electron*, vol. 31, no. 10, pp. 6792–6796, Oct. 2016.
[22] X. Wang and F. Blaabjerg, "Harmonic stability in power electronic-based power systems: Concept, modeling, and analysis," *IEEE Trans. Smart Grid*, vol. 10, no. 3, pp. 2858–2870, May 2019.
[23] L. Harnefors, "Modeling of three-phase dynamic systems using complex transfer functions and transfer matrices," *IEEE Trans. Ind. Electron.*, vol. 54, no. 4, pp. 2239–2248, Aug. 2007.
[24] X. Wang, L. Harnefors, and F. Blaabjerg, "Unified impedance model of grid-connected voltage-source converters," *IEEE Trans. Power Electron.*, vol. 33, no. 2, pp. 1775–1787, Feb. 2018.
[25] C. Zhang, X. Cai, M. Molinas, and A. Rygg, "Frequency-domain modelling and stability analysis of a DFIG-based wind energy conversion system under non-compensated AC grids: Impedance modelling effects and consequences on stability," *IET Power Electron.*, vol. 12, no. 4, pp. 907–914, Apr. 2019.
[26] H. Liu, X. Xie, C. Zhang, Y. Li, and H. Liu, "Quantitative SSR analysis of series-compensated DFIG-based wind farms using aggregated RLC circuit model," *IEEE Trans. Power Syst.*, vol. 32, no. 1, pp. 474–483, Jan. 2017.
[27] A. Moharana, R. K. Varma, and R. Seethapathy, "SSR alleviation by STATCOM in induction-generator-based wind farm connected to series compensated line," *IEEE Trans. Sustain. Energy*, vol. 5, no. 3, pp. 947–957, Jul. 2014.
[28] L. Wang and D.-N. Truong, "Stability enhancement of a power system with a PMSG-based and a DFIG-based offshore wind farm using a SVC with an adaptive-network-based fuzzy inference system," *IEEE Trans. Ind. Electron.*, vol. 60, no. 7, pp. 2799–2807, Jul. 2013.
[29] L. Fan and Z. Miao, "Mitigating SSR using DFIG-based wind generation," *IEEE Trans. Sustain. Energy*, vol. 3, no. 3, pp. 349–358, Jul. 2012.
[30] H. A. Mohammadpour and E. Santi, "SSR damping controller design and optimal placement in rotor-side and grid-side converters of series-compensated DFIG-based wind farm," *IEEE Trans. Sustain. Energy*, vol. 6, no. 2, pp. 388–399, Apr. 2015.
[31] P.-H. Huang, M. El Moursi, W. Xiao, and J. Kirtley, "Subsynchronous resonance mitigation for series-compensated DFIG-based wind farm by using two-degree-of-freedom control strategy," *IEEE Trans. Power Syst.*, vol. 30, no. 3, pp. 1442–1454, May 2015.
[32] M. A. Chowdhury and G. M. Shafiullah, "SSR mitigation of series-compensated DFIG wind farms by a nonlinear damping controller using partial feedback linearization," *IEEE Trans. Power Syst.*, vol. 33, no. 3, pp. 2528–2538, May 2018.
[33] A. E. Leon and J. A. Solsona, "Sub-synchronous interaction damping control for DFIG wind turbines," *IEEE Trans. Power Syst.*, vol. 30, no. 1, pp. 419–428, Jan. 2015.
[34] J. Yao, X. Wang, J. Li, R. Liu, and H. Zhang, "Sub-synchronous resonance damping control for series-compensated DFIG-based wind farm with improved particle swarm optimization algorithm," *IEEE Trans. Energy Convers.*, vol. 32, no. 2, pp. 849–859, Jun. 2019.
[35] H. Baesmat and M. Bodson, "Suppression of sub-synchronous resonances through excitation control of doubly-fed induction generators," *IEEE Trans. Power Syst.*, to be published.
[36] I. Vieto and J. Sun, "Real-time simulation of subsynchronous resonance in type-III wind turbines," in *Proc. IEEE 15th Workshop Control Modeling Power Electron. (COMPEL)*, Jun. 2014, pp. 1–8.

XUEGUANG ZHANG (M'13) was born in Heilongjiang, China, in 1981. He received the B.S., M.S., and Ph.D. degrees in electrical engineering from the Harbin Institute of Technology, Harbin, China, in 2003, 2005, and 2010, respectively. Since 2015, he has been an Associate Professor with the Department of Electrical and Engineering, Harbin Institute of Technology. His current research interests include distributed generation and renewable energy conversion systems.

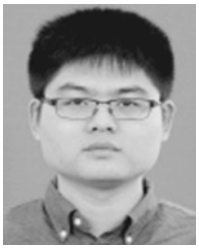

YAGE ZHANG was born in Nanyang, China, in 1996. He received the B.S. degree in electrical engineering from Harbin Engineering University, Harbin, China, in 2018. He is currently pursuing the M.S. degree in power electronics with the Harbin Institute of Technology, Harbin. His current research interests include modeling of Doubly-fed induction generator, their integration to the electric grid, and system stability analysis.

RAN FANG was born in Anqin, Anhui, China, in 1994. He received the M.S. degree in electrical engineering from the Harbin Institute of Technology, Harbin, China, in 2018. He is currently a Software Engineer with Delta Electronics, Inc. His current research interests include the stability analysis of grid-connected systems and the control of three phase converter.

DIANGUO XU (M'97–SM'12–F'17) was born in Heilongjiang, China, in 1960. He received the B.S. degree in control engineering from the Harbin Shipbuilding Engineering Institute, Harbin, China, in 1981, and the M.S. and Ph.D. degrees in electrical engineering from the Harbin Institute of Technology, Harbin, in 1984 and 1990, respectively. Since 1994, he has been a Professor with the Department of Electrical Engineering, Harbin Institute of Technology. His current research interests include robotics, lighting electronics, power quality mitigation, consumer electronics, power electronics, and motor drives. He is a member of the China Electrotechnical Society and China Power Supply Society.